

The impact of the interfacial Kapitza resistance on colloidal thermophoresis

Juan D. Olarte-Plata* and Fernando Bresme[†]
 Department of Chemistry, Imperial College London
 (Dated: July 20, 2023)

Thermal gradients impart a force on colloidal particles pushing the colloids towards cold or hot regions, a phenomenon called thermophoresis. Existing theories describe thermophoresis by considering the local perturbation of the thermal field around the colloid. While these approaches incorporate interfacial surface free energies, they have consistently ignored the impact of the Kapitza resistance associated with the colloid-solvent interface. We propose a theoretical approach to include interfacial Kapitza resistance effects, and we test the new equations using non-equilibrium molecular dynamics simulations. We demonstrate that the Kapitza resistance influences the local thermal field around a colloid, modifying the Soret coefficient. We conclude that interfacial thermal conductance effects must be included to describe thermophoresis.

Introduction: Thermophoresis describes the motion of colloidal particles in solution. This physical effect was discovered by Ludwig and Soret in the 19th century using alkali halide aqueous solutions [1, 2]. Thermophoresis is a complex non-equilibrium phenomenon whose explanation has motivated significant experimental and theoretical work [3–15]. Following the behavior observed in thermodiffusion, colloids can feature thermophobic behaviour at high temperature and thermophilic behaviour at low temperature. The temperature at which this transition takes place depends on the particle size [16] or screening length in charged colloids [8]. Duhr and Braun introduced the idea of solvation entropy and connected thermophoresis to interfacial properties [8], and Würger [6] developed a hydrodynamic theory where the colloid thermophoretic velocity depends on the solvent and colloid thermal conductivities, the temperature derivative of the solvent-colloid surface energy (surface entropy) and the solvent viscosity. Arango-Restrepo and Rubi [17] derived an equation for the Soret coefficient using the Faxén theorem. Their equation does incorporate the derivative of the interfacial tension with temperature and the viscosities of the fluid and the particle.

In most theoretical approaches referred to above, the thermophoretic force depends on the magnitude of the temperature gradient at the colloid surface. At the colloid-fluid interface, there are abrupt changes in the thermodynamic and transport properties, such as density and thermal conductivity. In the presence of a thermal gradient, these discontinuities give rise to the Kapitza resistance [18, 19] resulting in a temperature “jump” at the interface that might influence the thermal field around a colloid, potentially modifying the thermophoretic force. The impact of the Kapitza resistance, or the inverse quantity, the Interfacial Thermal Conductance (ITC), G_K , will depend on the magnitude of the conductances and, therefore, the colloid-solvent interfacial properties. High ITC will result in small temperature “jumps” at the colloid surface, but low ITC might lead to important differences in the interfacial temperatures of the colloid and the solvent. To understand what constitutes high or low ITC, it is instructive examining experimental studies of hydrophobic and hydrophilic interfaces using self-assembled monolayers [20]. The reported ITCs vary between $G_K = 50 \text{ MW}/(\text{K m}^2)$, “low”, and

$150 \text{ MW}/(\text{K m}^2)$, “high” ITC. Computer simulations of interfaces reported much lower ITC, $\sim 1 \text{ MW}/(\text{K m}^2)$ [21] for liquid-vapor interfaces, or higher ITCs $\sim 200\text{-}300 \text{ MW}/(\text{K m}^2)$ [22, 23] for the gold-water interface. For low ITC, $G \sim 10 \text{ MW}/(\text{K m}^2)$ measurable temperature differences between the solvent and the colloid, $\Delta T \sim 0.1 - 1 \text{ K}$, might appear for heat fluxes achievable in micro-fluidics ($\sim 10^6 \text{ K/m}$) [8] or plasmonic experiments (10^8 K/m) [24].

Here we extend previous theories of thermophoresis by incorporating ITC effects. We show that the ITC substantially modifies the temperature field around a colloid in solution and the colloidal thermophoretic force, particularly at low ITCs. We corroborate the general predictions of the theory using non-equilibrium molecular dynamics simulations.

The Theoretical Model: Several authors [25–28] derived equations for the Soret coefficient of spherical colloids by considering the deformation of the temperature field and the ensuing interfacial tension gradient around the colloid, which leads to a Marangoni force. The deformation of the temperature field emerges from the contrast of thermal conductivities of the solvent, κ^s , and that of the colloid, κ^c . For a spherical colloid immersed in an external temperature field ∇T , of magnitude $|\nabla T|$ in the \vec{x} direction, the temperature profile (in polar coordinates), far away from the particle is:

$$T^{ext} = T_0 + |\nabla T| \vec{x} = T_0 + |\nabla T| r \cos \theta \quad (1)$$

where T_0 is a reference temperature far from the colloid. Near the colloid, the solvent, $T^s(R, \theta)$ and colloid, $T^c(R, \theta)$ temperature profiles fulfill the boundary conditions:

$$T^s(R, \theta) = T^c(R, \theta) \quad (2)$$

$$\kappa^s \frac{\partial T^s(r, \theta)}{\partial r} \Big|_{r=R} = \kappa^c \frac{\partial T^c(r, \theta)}{\partial r} \Big|_{r=R} \quad (3)$$

Following [26–28] the solution of the Laplace equation is:

$$T^s(r, \theta) = T_0 + |\nabla T| r \cos \theta \left[1 + \alpha \left(\frac{R}{r} \right)^3 \right] \quad (4)$$

$$T^c(r, \theta) = T_0 + |\nabla T| r \cos \theta [1 + \alpha] \quad (5)$$

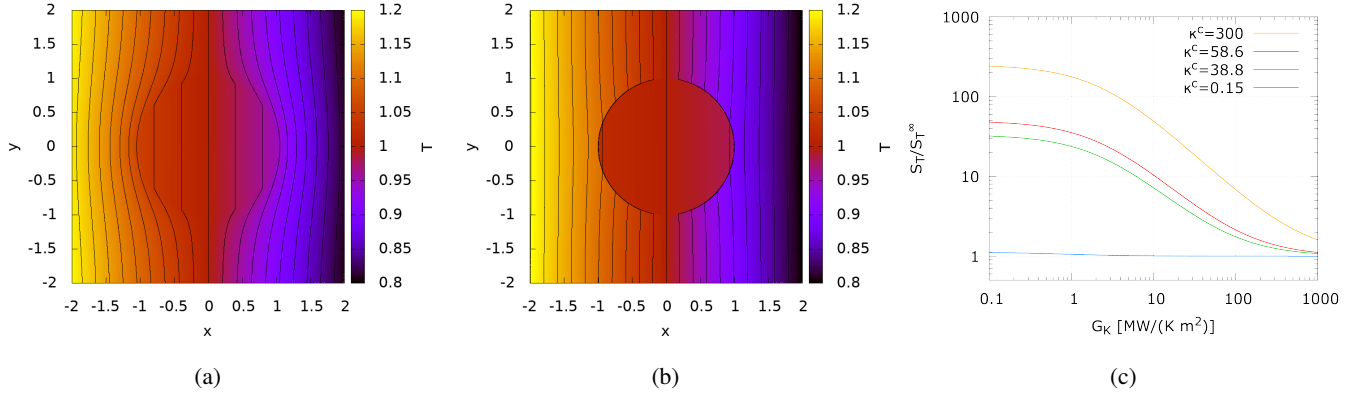


FIG. 1. Temperature field around a spherical colloid of radius $R = 1.0$, without (a) and with (b) interfacial thermal conductance effects. The results in panel (a) were obtained using Eqs. (4) and (5), and those in panel (b) with Eqs. (9) and (10). The results correspond to the thermal conductivities $\kappa^s = 1.0$, $\kappa^c = 4.0$, interfacial thermal conductance, $G_K = 1.0$, average temperature $T_0 = 1$, and temperature gradient $|\nabla T| = 0.1$. These reduced units are compatible with a colloid of radius 250 nm with $\kappa^c/\kappa^s = 4$ in water ($\kappa^s = 0.6$ W/(K m)), $G_K \sim 3$ MW/(K m²). (c) Predicted Soret coefficient as a function of the interfacial thermal conductance, G_K , for different colloid thermal conductivities (in units of W/(K m)) and $\kappa^s = 0.6$ W/(K m). The lines represent results obtained with Eq. (17). We have represented the Soret coefficient divided by the corresponding Soret coefficient, S_T^∞ when $G_K \rightarrow \infty$, *i.e.* when the ITC effects are neglected. The results for S_T^∞ were obtained using Eq. (15) and α (Eq.(6)) instead of α' .

where R is the colloid radius. The parameter α quantifies the thermal conductivity contrast between the colloid and the fluid. An explicit equation for α follows from the boundary condition in Eq. (3),

$$\alpha = \frac{\kappa^s - \kappa^c}{2\kappa^s + \kappa^c} \quad (6)$$

The solvent-colloid interface results in an interfacial thermal conductance that modifies the boundary conditions given by Eqs. (2) and (3), as the temperature features a discontinuous jump, $\Delta T = \frac{J_q}{G_K}$, defined by the heat flux, J_q , and the interfacial thermal conductance, G_K . The new boundary conditions, including G_K are,

$$T^{ls}(R, \theta) - \frac{\kappa^s}{G_K} \frac{\partial T^{ls}(r, \theta)}{\partial r} \Big|_{r=R} = T^{lc}(R, \theta) \quad (7)$$

$$\kappa^s \frac{\partial T^{ls}(r, \theta)}{\partial r} \Big|_{r=R} = \kappa^c \frac{\partial T^{lc}(r, \theta)}{\partial r} \Big|_{r=R} \quad (8)$$

where the prime indicates the equations include the interfacial thermal conductance effect. The solution of Eqs. (7) and (8) gives the corresponding temperature profiles,

$$T^{ls}(r, \theta) = T_0 + |\nabla T| r \cos \theta \left[1 + \alpha' \left(\frac{R}{r} \right)^3 \right] \quad (9)$$

$$T^{lc}(r, \theta) = T_0 + |\nabla T| r \cos \theta [1 + \alpha' + \beta'] \quad (10)$$

where α' and β' are

$$\alpha' = \frac{\kappa^s - \kappa^c(1 + \beta')}{2\kappa^s + \kappa^c} \quad (11)$$

$$\beta' = \frac{-3\kappa^s \kappa^c}{G_K R (2\kappa^s + \kappa^c) + 2\kappa^s \kappa^c}. \quad (12)$$

For $G_K \rightarrow \infty$, $\beta' \rightarrow 0$ and we recover Eqs. (4) and (5). We note that Eqs. (9) and (10) agree with those derived in reference [29] to obtain the effective thermal conductivity of composites.

Fig. 1 shows the temperature profiles around the colloid with and without interfacial thermal conductance effects. The ITC has a significant impact on the temperature field, and the temperature profile features a discontinuity for the solution that includes the ITC effects. Although the temperature field appears less deformed in the vicinity of the colloid, the ITC leads to different thermal fields far from the colloid surface. The changes in the thermal field influence the thermophoretic force, thermophoretic velocity, and ultimately the Soret coefficient. We now follow the approach introduced in reference [30] to address these changes. We obtain the thermophoretic velocity by considering the surface stress around the colloid. The drift velocity of the particle is given by (see section 1 in the SI for a derivation of the equations given below):

$$u = -\frac{\gamma_T R (1 + \alpha')}{3\eta} |\nabla T| \quad (13)$$

where η is the solvent viscosity and $\gamma_T = d\gamma/dT$ quantifies the change of the interfacial tension, γ , with temperature. In this

theory, the thermophoretic force is a Marangoni force emerging from the surface stress around the colloid due to the temperature gradient. The thermal diffusion coefficient is defined by the factor in front of the thermal gradient in Eq. (13)

$$D_T = \frac{\gamma_T R(1 + \alpha')}{3\eta} \quad (14)$$

which again reduces to the equations reported in previous work [6] when G_K is neglected. The Soret coefficient is given by $S_T = D_T/D$, where D is the interdiffusion coefficient approximated for highly diluted suspensions by the colloid diffusion coefficient. For a spherical colloid, $D = k_B T / (\xi \pi \eta R)$, where ξ is a numerical parameter accounting for the boundary conditions. The Soret coefficient is given by:

$$S_T = 4\pi R^2 \frac{(1 + \alpha')\gamma_T}{3k_B T} + \frac{1}{T}, \quad (15)$$

where the α' parameter considers the different thermal conductivities of the solvent and colloid and the interfacial thermal conductance. The second term of Eq. (15) represents the ideal contribution to the Soret coefficient. The origin of the factor “4” in Eq. (15) is justified in the derivation included in the SI (see section 2).

The scaling of the Soret coefficient with the square of the colloid radius (R^2) and the inverse of the temperature is consistent with previous computations of Soret coefficients [31]. However, α' introduces an additional dependence on the colloid radius through Eq. (12). The solution, including G_K for the solvent and colloid temperature profiles, results in a larger deformation of the temperature field far from the particle (see Figures 1a,b) and a temperature discontinuity at the colloid surface. Based on Eq. (12), we expect that the impact of the interfacial thermal conductance on the Soret coefficient will be stronger when the thermal conductivities of the solvent and the colloid are very different. Figure 1c illustrates the impact of G_K on the predicted Soret coefficient for a colloid of radius $R = 250$ nm immersed in water with $\kappa^s = 0.6$ W/(K m). For the colloid, we consider a range of thermal conductivities, $\kappa^c = 0.15 \dots 300$ W/(K m). The intermediate thermal conductivities, 58.6 and 38.8 W/(K m), might be representative of the thermal conductivity of a gold nanoparticle coated with a 1 nm or 2 nm alkane passivating layer, with a thermal conductivity for the layer of 0.45 W/(K m)[32] (see SI section 7, for more details). We also consider the thermal conductivity of a colloid made of polystyrene with $\kappa^c = 0.15$ W/(K m) as well as high thermal conductivity, of the order of that of bulk gold, $\kappa^c = 300$ W/(K m). The range of ITCs represented in Figure 1c, covers values corresponding to liquid-vapour interfaces 1 MW/(K m²) [33], and hydrophobic and hydrophilic self assembled monolayers (50-1000 MW/(K m²)) [20, 32]. For similar solvent and colloid thermal conductivities, the impact of G_K is relatively small, and the results converge to the previous solution that assumes $G_K \rightarrow \infty$. The convergence is much slower when κ^s and κ^c are very different. Moreover,

at low G_K , the difference in the Soret coefficient is significant, even for interfacial thermal conductances corresponding to hydrophobic layers, ~ 50 MW/(K m²). In summary, our results show that low ITCs can significantly enhance the Soret coefficient when the thermal conductivity of the colloid is much higher than the thermal conductivity of the solvent.

We have shown that the Soret coefficient is proportional to the parameter $1 + \alpha'$. We now extend the analysis of the dependence of the system by introducing the dimensionless quantities $\lambda = \kappa^s / \kappa^c$ and $\varepsilon = G_K R / \kappa^s$. The first quantity is simply the ratio between the thermal conductivities of the solvent and the colloid, while the latter relates the interfacial thermal resistance of the interface with that of the fluid. Using these definitions, we can express the parameter $1 + \alpha'$ as:

$$1 + \alpha' = \frac{3\lambda + \frac{3}{\varepsilon(2\lambda + 1) + 2}}{2\lambda + 1} \quad (16)$$

The solution when $\varepsilon \rightarrow \infty$ converges to $1 + \alpha = 3\lambda / (2\lambda + 1) = 3\kappa^s / (2\kappa^s + \kappa^c)$. The ratio between the solutions with and without considering the ITC can be written as:

$$\frac{S_T}{S_T^\infty} = \frac{1 + \alpha'}{1 + \alpha} = 1 + \frac{1}{\lambda \varepsilon (2\lambda + 1) + \lambda} \quad (17)$$

where S_T^∞ is the Soret coefficient for $G_K \rightarrow \infty$.

Test of the theoretical model using computer simulations: To test the theoretical predictions, we performed computer simulations of a coarse-grained colloid immersed in a WCA solvent at reduced density, $\rho = 0.8$ (see SI for more details on the simulation setup and model). The WCA inter-particle interactions are repulsive, and we also use this model to calculate the fluid-colloid interactions. The inter-particle interactions inside the colloid are described with a spherically truncated and shifted Lennard-Jones potential with interaction strengths varying between $\varepsilon_c / \varepsilon_s = 20 \dots 100$, where ε_s is the interaction strength between solvent particles.

We used two different simulation geometries to test the theoretical predictions discussed above. G_K , κ^s and κ^c were obtained using a *radial heat flux* simulation set-up (see Fig. 2-c). The deformation of the temperature field due to the presence of the spherical particle was studied using an *external gradient* set-up (see Fig. 2-a,b). In both set-ups, thermal gradients are simulated explicitly by setting hot and cold boundaries (see Fig. 2). The *external gradient* set-up was also employed to compute the thermal conductivity of the solvent and the Soret coefficient by computing the thermophoretic force associated with the displacement of the colloids attached with a harmonic spring to the geometric centre of the reservoirs shown in Fig. 2-a,b (see e.g. ref.[15] for details on this method). The thermal conductivity and interfacial thermal conductance were obtained from the heat flux using Fourier’s law, $J_q = -\kappa \nabla T$ and the Kapitza relation, $J_q = G_K \Delta T$, where ∇T is the thermal gradient, and ΔT the temperature “jump” at the colloid-

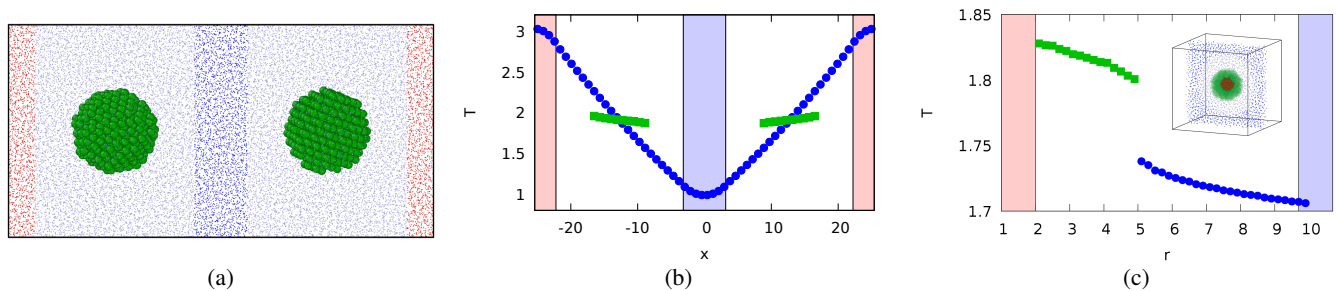


FIG. 2. (a) Snapshot of the simulation box in the *external gradient* set-up, showing the thermostating regions (red-hot, blue-cold). The solvent particles are represented as blue dots for visualization purposes, and the colloid as green spheres. (b) Temperature profile for a system with $\epsilon_c/\epsilon_s = 20$, showing the temperature of the fluid (blue circles) and the colloid (green squares). (c) Temperature profile for the *radial heat flux* system with $\epsilon_c/\epsilon_s = 20$, showing the temperature of the fluid (blue circles) and the spherical particle (green squares), and the corresponding temperature jump. The inset shows a snapshot of the simulation box, highlighting the thermostatted core (red) and the surrounding solvent (blue dots).

solvent interface (see Fig. 2-c). Further simulation details are provided in the SI (see section 3).

First, we compare the predicted field around the spherical colloid against the simulated data, using Eqs. (4) and (5), replacing α by α' to include ITC effects (see SI for details on the computation of the temperature field using NEMD simulations). We find good agreement between the predictions of the analytical solution and the NEMD results (see Fig. 3). The NEMD results show some deviations at the colloid surface, which are connected to the granularity of the colloid surface. Away from the interfacial region, the agreement of the temperature isolines is good, showing Eqs. (4) and (5) capture the deformation of the solvent temperature field. The impact of the interfacial thermal conductance on the deformation of the temperature field is also evident (c.f. Figs.3-a, b and c). The temperature field features a stronger deformation with decreasing ITC. Both the analytical and simulation results indicate that ITC effects are needed to describe temperature fields around colloids. As shown in Fig. 3, the impact of G_K is significant at distances > 5 solvent molecular diameters.

We discuss now the dependence of the Soret coefficient with the ITC. To address this point, we vary G_K keeping the solvent-particle interaction strength constant and approximately the same interfacial temperature; hence γ_T does not change with G_K . This notion is supported by the lack of dependence of the colloid solvation structure with ϵ_c (see Fig. S1 in the SI). We isolate G_K and surface tension effects by modifying the colloid particle-particle interactions. This leads to a systematic change of the colloid vibrational density of states (VDoS) relative to the VDoS of the solvent. By changing the overlap of the two VDoS we achieve higher or lower G_K , and we can systematically test Eq. (15). Figure 4-a shows the impact of the ϵ_c on the overlapping of the colloid and solvent VDoS. The ITC decreases with increasing ϵ_c due to a shift of the colloid VDoS to higher frequencies as ϵ_c increases (see Fig S3 in the SI).

The thermal conductivity of the colloid appearing in Eq. (15) was computed by using the radial heat flux setup (see Fig. 2-c). We used Fourier's law by fitting the temperature

gradient inside the colloid in an interval far from the colloid surface to avoid including interfacial effects (see section 6 in the SI for details). In the SI, we show in Fig. S5 that the colloid thermal conductivities decrease with increasing ϵ_c . These thermal conductivities were used as input for Eq. (15). The final element needed to test Eq. (15) is the Soret coefficient.

The computation of the Soret coefficient using the setup in Figure 2a involves restraining the translational motion of the colloid with a spring, and this results in a hydrodynamic flow[15, 34] around the nanoparticle that leads to a system size dependent Soret coefficient. However, for a given system size, the Soret coefficient with this approach agrees with the one corresponding to a freely drifting particle [11], as described in Eq. (15). Hence, we computed the Soret coefficient for system sizes corresponding to $L_{y,z} = 16$ and 20. To test the numerical results against the theory given by Eq. (15) we used the nanoparticle and solvent thermal conductivities corresponding to the bulk regions, the ITC obtained with the radial heat flux method (see Fig.2c), and the nanoparticle radius, $R = 5$. We set a constant fitting parameter in Eq. (15), $c = 4\gamma_T \chi_{L_{y,z}}$, where $\chi_{L_{y,z}}$ takes into account the finite size of the simulation box and its impact on the Soret coefficient.

Figure 4b shows the dependence of the simulated Soret coefficients with G_K . This general behaviour agrees with the theoretical results predicted by Eq. (15) and shown in Figure 1c, namely the Soret coefficient decreases with increasing G_K . We find that Eq. (15) reproduces the trends of the simulated Soret coefficients, but some deviations are evident at large G_K . We note that in the theoretical calculation we used the bulk solvent thermal conductivities. However, the solvent does not reach bulk behavior until a distance of ~ 2 molecular diameters from the colloid surface (see Fig. S1 in the SI). Hence, we recalculated the solvent thermal conductivity, including only the region within two molecular diameters from the colloid surface. The thermal conductivity of this layer is lower than the bulk one (see Fig. S4 in the SI), and we find it provides better agreement between the simulation data and the theory (see Fig. 4b).

Final remarks: In this work, we have extended previous

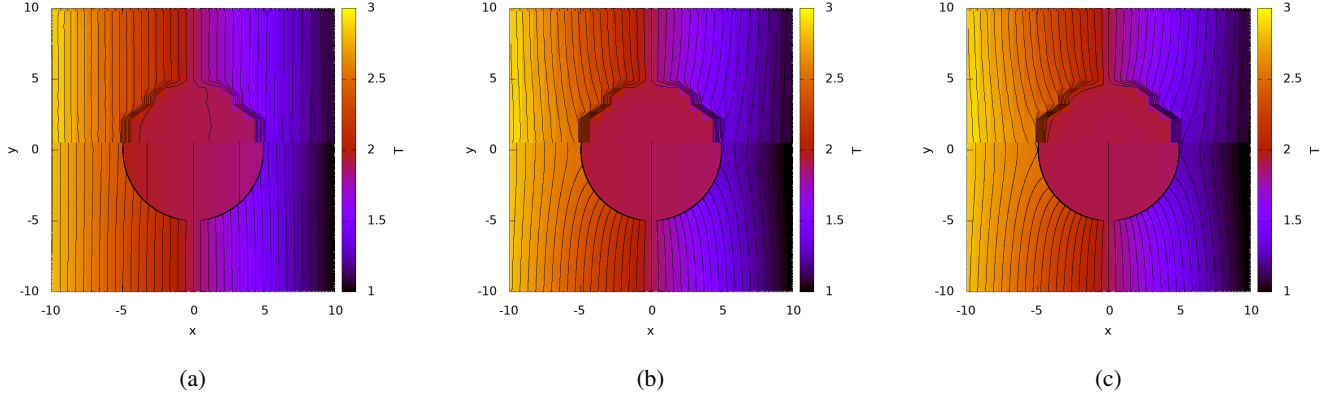


FIG. 3. Overlay of the NEMD simulation ($y > 0$) and analytical results ($y < 0$), for $\epsilon_c/\epsilon_s = 20, 60, 100$ corresponding to three interfacial thermal conductances, 1.4 (a), 0.3 (b) and 0.11 (c), and colloid thermal conductivities of $\kappa^c = 36$ (a), $\kappa^c = 28$ (b) and $\kappa^c = 20.5$ (c) (see SI for details regarding calculations of the thermal conductivities). All the results were obtained using $\kappa^s = 6.87$, $T_0 = 1.9$ and $|\nabla T| = 0.09$.

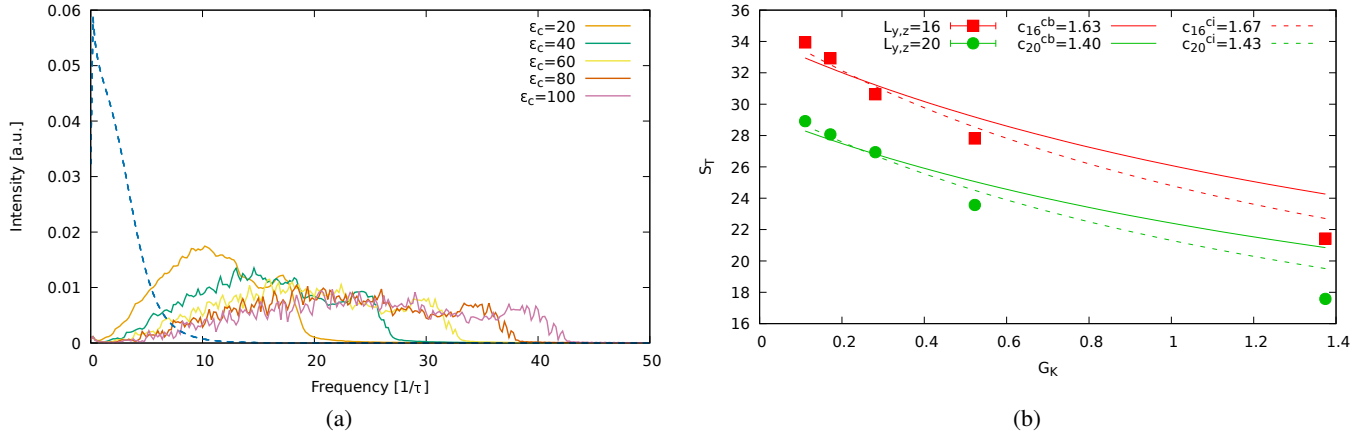


FIG. 4. (a) VDoS of the colloid as a function of ϵ_c . The fluid VDoS is represented with blue dashed lines. (b) Soret coefficient as a function of G_K and system size. The solid lines represent fittings using the bulk thermal conductivity of the fluid (with fitting parameter denoted by cb), while the dashed lines represent fittings to Eq. (15) using the interfacial thermal conductivity of the fluid (with fitting parameter denoted by ci). In both cases, the nanoparticle core thermal conductivity was used.

theories of the Soret effect [25–28], and presented the analytical solution to the temperature field around a spherical colloid including the Kapitza resistance contribution to account for the temperature discontinuity at the colloid-solvent interface. In this new formulation the magnitude of the Soret coefficient is determined by the deformation of the thermal field associated to the thermal conductivity of the colloid and the solvent, the interfacial thermal conductance, and the stress around the surface of the colloid, which translates into a Marangoni type force. The resulting equation is similar in structure to previous ones, but the thermal conductivity terms are corrected to account for the interfacial thermal conductance, G_K . We have shown that G_K significantly impacts the Soret coefficient when G_K is $< 100 - 300 \text{ W}/(\text{K m}^2)$, and the colloid thermal conductivity is much higher than the one of the solvent ($k_c \gg k_s$), such as in gold nanoparticle suspensions. For $k_c \sim \kappa_s$ (e.g. polymer nanoparticles) the impact of

G_K is small, and for $G_K \rightarrow \infty$, *i.e.* highly thermally conductive surfaces, we recover previous equations, which ignored G_K effects. We have verified the analytical equations by using non-equilibrium molecular dynamics computer simulations of coarse-grained models of colloids immersed in a solvent. The simulated temperature fields show good agreement with the “continuum” theory, and the Soret coefficient varies with G_K as predicted theoretically.

In addition to proposing new analytical equations to describe the Soret effect, our work highlights the importance of the Kapitza resistance in determining the thermophoresis of colloidal particles. This contribution has been ignored before, but as demonstrated here, it can influence the temperature field around a colloid and the thermophoretic force. We propose that ITC effects must be included to describe thermophoresis in terms of interfacial properties. We believe that the ideas presented in this work should prove helpful to advance the

description of thermophoresis, which is a very complex non-equilibrium coupling effect with potential applications to colloidal trapping, nanofluidics, and the design of analytical devices.

We thank the Leverhulme Trust for grant RPG-2018-384 and the Imperial College High Performance Computing Service for providing computational resources.

DATA AVAILABILITY STATEMENT

The data that support the findings of this study are available within the article [and its supplementary material].

* j.olarte@imperial.ac.uk

† f.bresme@imperial.ac.uk

- [1] C. Ludwig, Sitzber. Akad. Wiss. Wien Math.-naturw. Kl. **20**, 539 (1856).
- [2] C. Soret, Arch. Sci. Phys. Nat. Geneve **2**, 48 (1879).
- [3] S. Wiegand, *Journal of Physics: Condensed Matter* **16**, R357 (2004).
- [4] S. Semenov and M. Schimpf, *Phys. Rev. E* **69**, 011201 (2004).
- [5] S. A. Putnam and D. G. Cahill, *Langmuir* **21**, 5317 (2005).
- [6] A. Würger, *Phys. Rev. Lett.* **98**, 138301 (2007).
- [7] R. Piazza and A. Parola, *Journal of Physics: Condensed Matter* **20**, 153102 (2008).
- [8] S. Duhr and D. Braun, *Proceedings of the National Academy of Sciences* **103**, 19678 (2006), <https://www.pnas.org/content/103/52/19678.full.pdf>.
- [9] G. Galliero and S. Volz, *The Journal of Chemical Physics* **128**, 064505 (2008), <https://doi.org/10.1063/1.2834545>.
- [10] H. Brenner, *Phys. Rev. E* **82**, 036325 (2010).
- [11] D. Lüsebrink, M. Yang, and M. Ripoll, *Journal of Physics: Condensed Matter* **24**, 284132 (2012).
- [12] J. Burelbach, M. Zupkauskas, R. Lamboll, Y. Lan, and E. Eiser, *The Journal of Chemical Physics* **147**, 094906 (2017), <https://doi.org/10.1063/1.5001023>.
- [13] A. Arango-Restrepo and J. M. Rubi, *The European Physical Journal E* **42**, 55 (2019).
- [14] J. D. Olarte-Plata and F. Bresme, *Phys. Chem. Chem. Phys.* **21**, 1131 (2019).
- [15] F. Bresme, J. D. Olarte-Plata, A. Chapman, P. Albella, and C. Green, *Eur. Phys. J. E* **45**, 59 (2022).
- [16] M. Braibanti, D. Vigolo, and R. Piazza, *Phys. Rev. Lett.* **100**, 108303 (2008).
- [17] Arango-Restrepo, Andrés and Rubi, J. Miguel, *Eur. Phys. J. E* **42**, 55 (2019).
- [18] P. L. Kapitza, *Phys. Rev.* **60**, 354 (1941).
- [19] E. T. Swartz and R. O. Pohl, *Rev. Mod. Phys.* **61**, 605 (1989).
- [20] Z. Ge, D. G. Cahill, and P. V. Braun, *Phys. Rev. Lett.* **96**, 186101 (2006).
- [21] J.-M. Simon, S. Kjelstrup, D. Bedeaux, and B. Hafskjold, *The Journal of Physical Chemistry B* **108**, 7186 (2004).
- [22] H. Bhattarai, K. E. Newman, and J. D. Gezelter, *The Journal of Chemical Physics* **153**, 204703 (2020), <https://doi.org/10.1063/5.0027847>.
- [23] J. D. Olarte-Plata and F. Bresme, *The Journal of Chemical Physics* **156**, 204701 (2022), <https://doi.org/10.1063/5.0090983>.
- [24] A. O. Govorov, W. Zhang, T. Skeini, H. Richardson, J. Lee, and N. A. Kotov, *Nanoscale Research Letters* **1**, 84 (2006).
- [25] A. Würger, *Phys. Rev. Lett.* **98**, 138301 (2007).
- [26] J. Giddings, P. M. Shinudu, and S. N. Semenov, *Journal of Colloid and Interface Science* **176**, 454 (1995).
- [27] P. Gaspard and R. Kapral, *Journal of Statistical Mechanics: Theory and Experiment* **2019**, 074001 (2019).
- [28] T. Bickel, G. Zecua, and A. Würger, *Phys. Rev. E* **89**, 050303 (2014).
- [29] D. Hasselman and L. F. Johnson, *Journal of Composite Materials* **21**, 508 (1987), <https://doi.org/10.1177/002199838702100602>.
- [30] A. Würger, *Phys. Rev. Lett.* **116**, 138302 (2016).
- [31] J. D. Olarte-Plata and F. Bresme, *The Journal of Chemical Physics* **152**, 204902 (2020), <https://doi.org/10.1063/5.0008237>.
- [32] J. D. Olarte-Plata, J. Gabriel, P. Albella, and F. Bresme, *ACS Nano* **16**, 694 (2022).
- [33] J. Muscatello, E. Chacón, P. Tarazona, and F. Bresme, *Phys. Rev. Lett.* **119**, 045901 (2017).
- [34] M. Yang and M. Ripoll, *Soft Matter* **9**, 4661 (2013).
- [35] L. D. Landau and E. M. Lifshitz, *Fluid Mechanics, Second Edition: Volume 6 (Course of Theoretical Physics)*, 2nd ed., Course of theoretical physics / by L. D. Landau and E. M. Lifshitz, Vol. 6 (Butterworth-Heinemann, 1987).
- [36] J. Morthomas and A. Würger, *Phys. Rev. E* **81**, 051405 (2010).
- [37] S. Plimpton, *Journal of Computational Physics* **117**, 1 (1995).
- [38] A. Stukowski, *MODELLING AND SIMULATION IN MATERIALS SCIENCE AND ENGINEERING* **18** (2010), 10.1088/0965-0393/18/1/015012.
- [39] D. Hasselman and L. F. Johnson, *Journal of Composite Materials* **21**, 508 (1987), <https://doi.org/10.1177/002199838702100602>.

SUPPLEMENTARY INFORMATION

1. DERIVATION OF THE EQUATIONS DISCUSSED IN THE MAIN TEXT

We follow the approach of Würger to describe the relation between the surface stress and the Marangoni force. The temperature gradient on the surface of the particle can be written as [25]:

$$\nabla_{\parallel} T = \left(\frac{1}{r} \frac{\partial T(r, \theta)}{\partial \theta} \right) \Big|_{r=R} = -|\nabla T| \sin \theta (1 + \alpha) \mathbf{t} \quad (18)$$

where \mathbf{t} is the tangential vector at the surface. The Marangoni force is given by [25]:

$$\nabla_{\parallel} \gamma = \gamma_T \nabla_{\parallel} T \quad (19)$$

where the Marangoni parameter is defined as the derivative of the interfacial free energy, γ , with respect to the temperature, $\gamma_T = d\gamma/dT$. The dissipative part of the stress tensor, σ' , is given by [25]:

$$\sigma'_{rr} = 2\eta \frac{\partial \hat{v}_r}{\partial r} \quad (20)$$

$$\sigma'_{r\theta} = \eta \left(\frac{1}{r} \frac{\partial \hat{v}_r}{\partial \theta} + \frac{\partial \hat{v}_\theta}{\partial r} - \frac{\hat{v}_\theta}{r} \right) \quad (21)$$

where η is the viscosity of the fluid. \hat{v}_r and \hat{v}_θ are the radial and tangential components of the fluid velocity field near the particle, in the particle frame of reference.

For a particle drifting with velocity $\mathbf{u} = u\hat{x}$ (due to the thermophoretic force), the solution to the Stokes equation for an incompressible fluid, $\eta \nabla^2 \hat{\mathbf{v}} = \nabla P$, can be written as [25]:

$$\hat{v}_r = -u \cos \theta \left(1 - \frac{R^3}{r^3} \right) \quad (22)$$

$$\hat{v}_\theta = u \sin \theta \left(1 + \frac{R^3}{2r^3} \right) \quad (23)$$

For this case, the tangential component of the stress tensor evaluated at the particle surface is:

$$\sigma'_{r\theta} \Big|_{r=R} = \frac{-3\eta u \sin \theta}{R} \quad (24)$$

The thermophoretic velocity of the particle can be found by balancing the tangential component of the stress tensor with the Marangoni force, $\sigma'_\theta \mathbf{t} = -\gamma_T \nabla_{\parallel} T$ [25], giving:

$$\frac{-3\eta u \sin \theta}{R} = \gamma_T |\nabla T| \sin \theta (1 + \alpha) \quad (25)$$

The drift velocity of the particle can thus be written as:

$$u = -\frac{\gamma_T R (1 + \alpha')}{3\eta} |\nabla T| \quad (26)$$

2. FORCES ON A FIXED PARTICLE

The total force on the particle is given by [35]

$$F_{tot} = \int_S (-p \cos \theta + \sigma'_{rr} \cos \theta - \sigma'_{r\theta} \sin \theta) dA \quad (27)$$

where p is the pressure, and σ'_{ij} are components of the stress tensor.

For the fixed particle, the fluid velocity can be written as [36]:

$$v_r = u_0 \cos \theta \left(\frac{R}{r} - \frac{R^3}{r^3} \right) \quad (28)$$

$$v_\theta = -\frac{u_0 \sin \theta}{2} \left(\frac{R}{r} + \frac{R^3}{r^3} \right) \quad (29)$$

In this case, u_0 represents the slip velocity at the surface of the particle. With these expressions for the velocity field, we arrive to:

$$\sigma'_{rr} \Big|_{r=R} = 4\eta \frac{u_0}{R} \cos \theta \quad (30)$$

$$\sigma'_{r\theta} \Big|_{r=R} = 3\eta \frac{u_0}{R} \sin \theta \quad (31)$$

The corresponding contributions to the total force are given by:

$$F_{\sigma'_{rr}} = \frac{16\pi}{3} \eta R u_0 \quad (32)$$

$$F_{\sigma'_{r\theta}} = -8\pi \eta R u_0 \quad (33)$$

The pressure contribution to the total force can be found from the following expression [6]:

$$P = P_0 + 2\alpha \cos \theta \frac{\eta u_0 R}{r^2} \quad (34)$$

where $\alpha = 1/2$ corresponds to the solution for the fluid velocity field around the fixed particle. The pressure contribution to the total force thus reads:

$$F_P = -\frac{4\pi}{3} \eta R u_0 \quad (35)$$

The total force on the particle is thus given by:

$$F_{total} = F_{\sigma'_{rr}} + F_{\sigma'_{r\theta}} + F_P = -4\pi \eta R u_0 \quad (36)$$

3. SIMULATION DETAILS

The fluid, with reduced density $\rho = \rho_n \sigma^3 = 0.8$ (ρ_n is the number density in particles/m⁻³) was described using the WCA model, *i.e.* a Lennard-Jones 12-6 potential with a cut-off radius corresponding to the minimum of the potential, *i.e.* $r_c = r_0 = 2^{1/6} \sigma$, with $\epsilon_s = 1.0$. σ is the diameter of the solvent and the particles inside the colloid. We used reduced units, $r = r_{SI}/\sigma$, $T = k_B T_K/\epsilon_s$, where r_{SI} is the distance in SI units, ϵ_s is the interaction strength between solvent particles and T_K the temperature in Kelvin. All the solvent-particle interactions were computed using the WCA model. The interactions between the particle inside the colloids, were described using a strongly attractive Lennard-Jones potential with a cut-off radius $r_c = 2.5\sigma$.

The simulations were run with a timestep $\delta t = 0.0025$ using LAMMPS [37]. After 10^4 timesteps in the NVT ensemble with $T = 1.0$, the thermostats (see Figure 2 in the main text) were activated. The first 10^5 timesteps were discarded before sampling for an additional 10^7 timesteps. The results reported in our work were obtained using 20 independent replicas, starting from random atomic velocities and colloid orientations.

To perform the simulations using the two setups discussed in the main paper (see Fig. 2), we generated cubic (*radial heat flux*) or rectangular (*external gradient*) simulation boxes with volume $V = (8a_0) \times (8a_0) \times (8a_0)$ or $V = (16a_0) \times (8a_0) \times (8a_0)$, where $a_0 = 2^{2/3} \sigma$ is the FCC lattice parameter of a solid with $\rho^* = 1.0$. To investigate finite-size effects in the computations of the Soret coefficient, we also simulated systems with $L_x = 20, 24, 28$ and $32a_0$ for the *external gradient* set-up. In all cases, $L_x = 2L_{y,z}$. To set a temperature gradient, hot and cold thermostating regions were defined at the centre and edges of the simulation box. The thermostating regions correspond to a spherical core, $r < 2.0\sigma$, and shell, $R > 9.7\sigma$ (*radial heat flux*), or rectangular slabs of width $4a_0$ (*external gradient*). Within these regions, the velocities of the fluid particles were rescaled to the target temperatures every 100 timesteps. The centre-of-mass momentum was also removed with the same frequency in order to prevent a drift in the translational motion of the atoms. The *external gradient* configuration generates two temperature gradients in opposite directions. A spherical particle, cut from an FCC lattice with density $\rho = 1.0$ and radius $R = 5\sigma$, was placed in the centre of each compartment, and attached with a harmonic potential, given by $U(r) = 0.5 k(r - r_0)^2$, with force constant $k = 10^3$. Snapshots of the simulation box, as well as a typical temperature profiles, are shown in Fig. 2. All the visualization were done using OVITO [38].

The temperature fields were calculated by dividing the simulation box in cubic voxels of volume $\sim (0.79\sigma)^3$, where the local temperature was sampled. In order to exploit the symmetry of the problem and improve sampling, the data was rebinned (using a weighted average) to (x, r) coordinates, where $r = \sqrt{y^2 + z^2}$. The bin size for the r coordinate was $\sim 0.56\sigma$.

The contours were generated using a linear interpolation, with increasing levels of 0.05.

4. DENSITY PROFILES OF THE FLUID

Fig. 5 shows the radial density profile of the fluid as a function of the colloid interaction strength, obtained under equilibrium conditions at $T = 2.0$. The results in Fig. S1 show that the colloid interactions have no impact on the density profiles of the solvent surrounding the colloid.

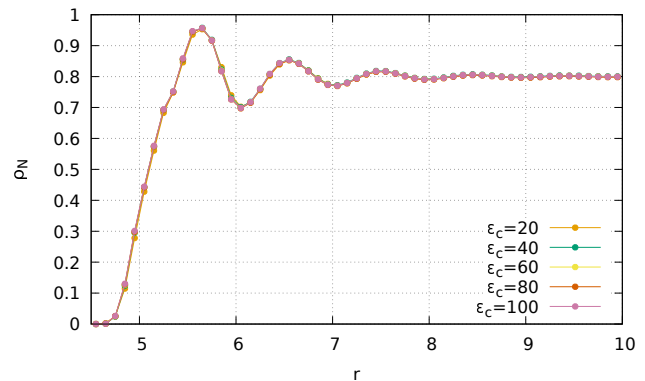


FIG. 5. Solvent radial density profiles around the colloid, as a function of the colloid interaction strength. The profiles were obtained at equilibrium conditions and $T = 2.0$.

5. CALCULATION OF THE COLLOID-SOLVENT INTERFACIAL THERMAL CONDUCTANCE, G_K

To compute the interfacial thermal conductance G_K we performed simulations targeting the highest and lowest interfacial temperatures obtained in the simulations of the Soret coefficient (see Fig. 2b in the main paper). Our simulations also take into account the rectification of the G_K , namely, the solvent is hotter or colder on both sides of the colloid (see Fig. 2b in the main text).

We compute the interfacial thermal conductance of uniform nanoparticles as a function of their internal interaction strength using the *radial heat flux* simulation set-up (see Fig 2c in the main paper). The temperature of the colloid core is thermostatted to a target temperature $T_c = 1.9$. The temperature of the bulk solvent is varied between $T_s = 1.7$ and $T_s = 2.1$ to account for the colloid-solvent contact on the hot and cold regions (see Figure 2b in the main text). For the calculation of the temperature “jump”, we fitted the temperature profiles using the heat diffusion equation near the interfacial region (see Figure S2). The range of radial distance for the colloid was restricted to $r_c^* = [4.0, 5.0]$, while for the solvent we used the interval $r_s = [5.0, 6.0]$.

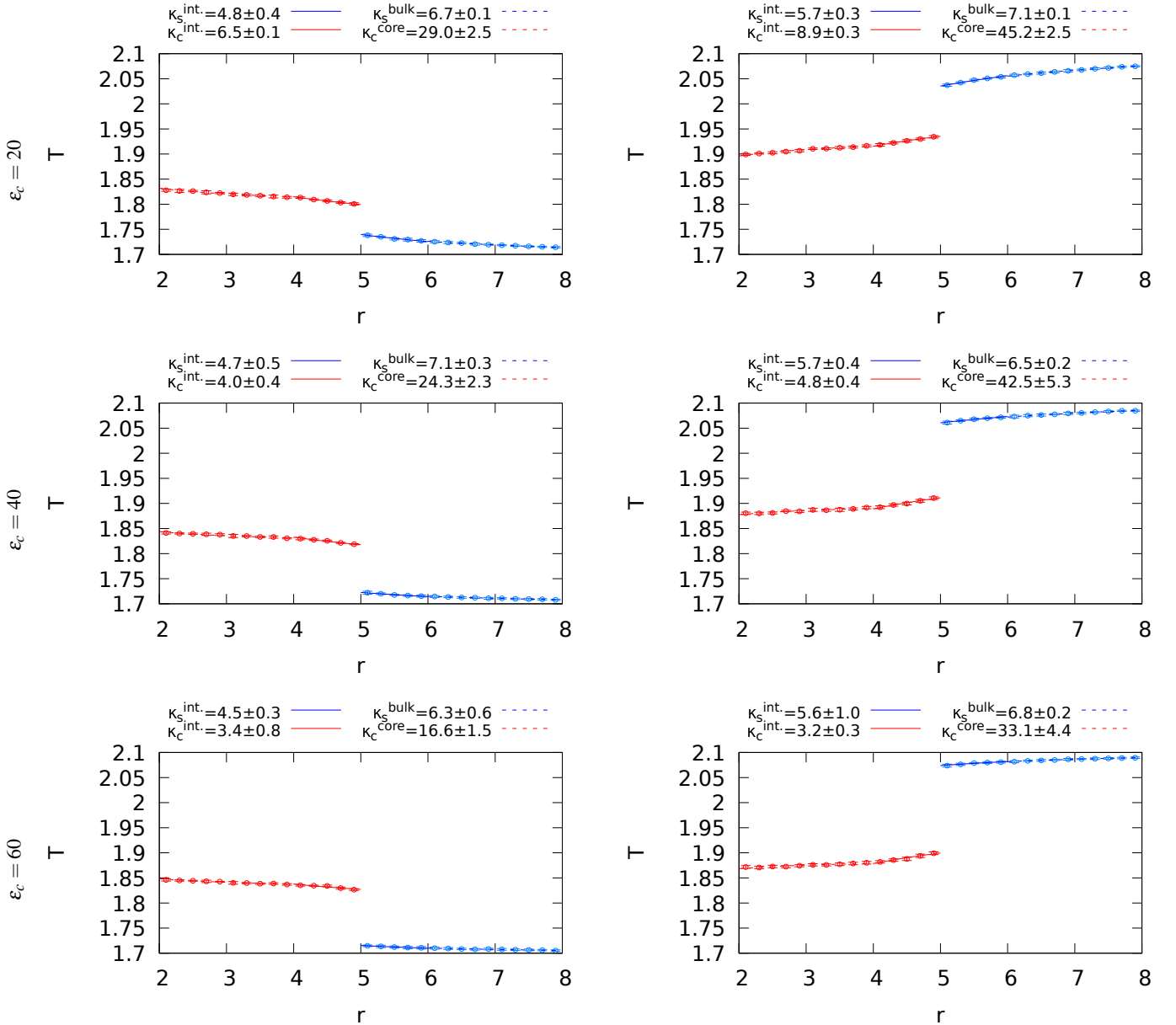


FIG. 6. Temperature profiles in the *radial heat flux* configuration, for different boundary conditions and colloid interaction strengths. The lines represent the fitting used to calculate the thermal gradient and thermal conductivities. κ_α^β refers to the colloid ($\alpha = c$) or solvent ($\alpha = s$) thermal conductivity obtained using the $\beta =$ “bulk” for the solvent, $\beta =$ “core” for the colloid or interfacial region $\beta =$ “int” for the solvent. Error bars represent the standard deviation, calculated from the individual temperature profiles of 10 replicas.

6. THERMAL CONDUCTIVITY OF THE SOLVENT AND COLLOID

The thermal conductivity of the solvent was calculated using the *radial heat flux* simulation set-up, and is shown in Fig. S4. Due to the decreasing heat flux with increasing particle interaction strength, we focused on the range $\epsilon_c = 20 - 60$. Fig. S4 shows the thermal conductivity as a function of the width of the fitting region and the boundary condition of the fluid. The thermal conductivity does not feature a signifi-

cant variation with either temperature or particle interaction strength ϵ_c . Hence, to plot the theoretical curves in Fig. 4 in the main text we used the thermal conductivities $\kappa_s^{\text{bulk}} = 6.87$ and $\kappa_s^{\text{int.}} = 5.16$ (see dashed horizontal lines in Fig. S4).

The thermal conductivity of the colloid (see Fig.9) was calculated using the *radial heat flux* simulation set-up. To assess interfacial effects on the thermal conductivity, we varied the width of the fitting region. We note that the thermal conductivity of the colloid decreases with increasing internal interaction strength. The larger interaction strengths were discarded due

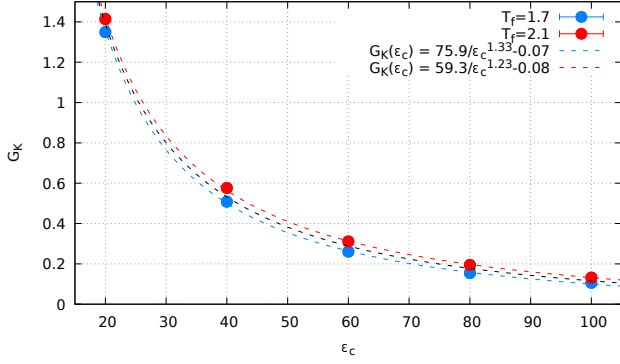


FIG. 7. Interfacial thermal conductance as a function of the colloid internal interaction strength, for different bulk fluid temperatures. The dashed lines indicate fittings to a function of the form $G(\epsilon_c) = a/\epsilon_c^b$.

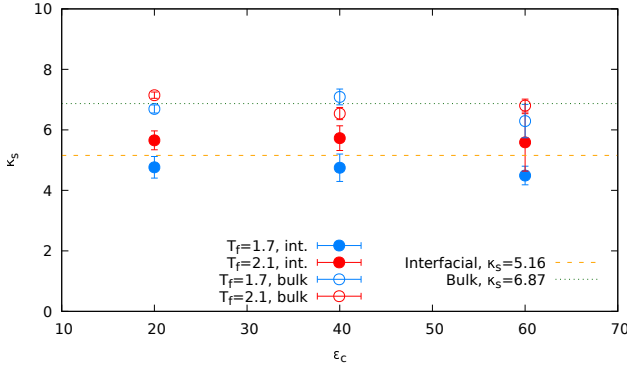


FIG. 8. Thermal conductivity of the solvent as a function of the colloid interaction strength and the temperature. The upper values where obtained using the temperature gradient in the bulk region, and the lower values were obtained using the interfacial temperature gradient (see Fig. S2 for definitions of bulk and interfacial regions). Red and blue points represent the thermal conductivity at different temperatures, targeting the temperatures at the hot or cold side of the colloid surface (see Figure 2b in the main text). The dashed horizontal lines represent the average of the thermal conductivities for each temperatures and varying ϵ_c .

to their low heat flux, which increases the uncertainty in the thermal conductivity.

Error bars for the thermal conductivities represent the asymptotic standard error from the fitting of the temperature profiles (and their associated standard deviations) shown in Fig. S2.

7. ESTIMATION OF THE EFFECTIVE THERMAL CONDUCTIVITIES OF FUNCTIONALIZED COLLOIDS

To estimate an effective thermal conductivity of the functionalised colloids discussed in in the main paper and of Fig.1c, we used the following approach. The effective ther-

mal conductivity of the colloid, κ_{eff} , can be estimated using the model introduced by Hasselman and Johnson [39], which reduces to the expression derived by Maxwell for infinite interfacial thermal conductance. As an example we consider here a gold colloid with $\kappa_{Au} \sim 300$ W/(K m), coated with an alkanethiol monolayer with $\kappa_m \sim 0.45$ W/(K m) [32] at ~ 300 K. The interfacial thermal conductance Au-monolayer interface is ~ 800 MW/(K m²)[32]. Following ref.[39] the effective thermal conductivity of the colloid

$$\kappa_{eff} = \kappa_m \frac{2 \left(\frac{\kappa_{Au}}{\kappa_m} - \frac{\kappa_{Au}}{RG_K} - 1 \right) V_{Au} + \frac{\kappa_{Au}}{\kappa_m} + \frac{2\kappa_{Au}}{RG_K} + 2}{\left(1 - \frac{\kappa_{Au}}{\kappa_m} + \frac{\kappa_{Au}}{RG_K} \right) V_{Au} + \frac{\kappa_{Au}}{\kappa_m} + \frac{2\kappa_{Au}}{RG_K} + 2} \quad (37)$$

where $V_{Au} = (R/(R+d))^3$ is the volume fraction of the gold particle with radius R , relative to the total volume of the colloid, defined by the radius $R+d$, where d is the thickness of the monolayer coating the gold core.

Considering a colloid of radius $R=250$ nm, and monolayers of thickness between 1 or 2 nm, we obtain the effective thermal conductivities 58.6 W/(K m) or 38.8 W/(K m), respectively. Ignoring the the interfacial thermal conductance, $G_K \rightarrow \infty$ we find that the effective thermal conductivity is higher, 83.0 and 48.2 W/(K m) for monolayer thicknesses of 1 or 2 nm, respectively.

8. Soret COEFFICIENT VS. INTERNAL INTERACTION STRENGTH AND SYSTEM SIZE

Fig. S6 shows the Soret coefficients obtained with the method discussed in section 2 above (see also discussion in the main paper pages 3 and 4). We considered difference colloid interaction strengths as well as different system sizes. The Soret coefficient decreases with increasing system size (see

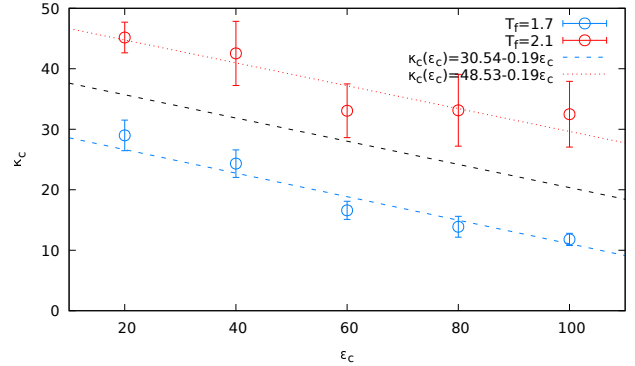


FIG. 9. Thermal conductivity of the colloid as a function of the colloid interaction strength, for different temperatures. The dashed lines indicate fittings to a linear function. The black dashed lines represent the average of both high and low temperature lines.

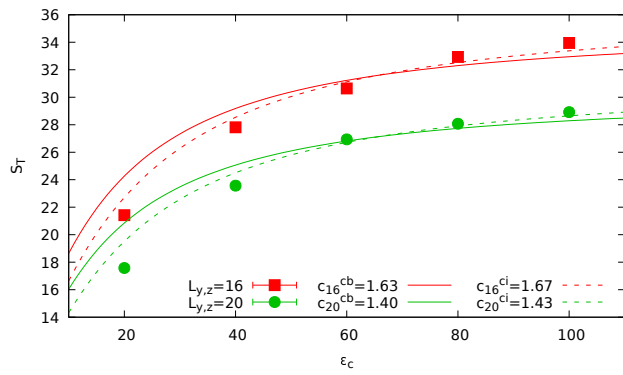


FIG. 10. Soret coefficient as a function of the particle interaction, ϵ_c , and system size. The symbols represent simulation results and the lines fittings to the theoretical equations. See discussion in the main text.

Fig. S6 and also the discussion on the truncation of the hydrodynamic field in reference[15]).